

<https://doi.org/10.1038/s41612-024-00597-2>

Intensified gradient La Niña and extra-tropical thermal patterns drive the 2022 East and South Asian “Seesaw” extremes

Check for updates

Peng Zhang¹, Bin Wang^{2,3}, Zhiwei Wu¹✉, Rui Jin⁴ & Can Cao¹

In July and August 2022, a notable “seesaw” extreme pattern emerged, characterized by the “Yangtze River Valley (YRV) drought” juxtaposed with the “Indus Basin (IB) flood”, leading to enormous economic and human losses. We observed that the “seesaw” extreme pattern concurs with the second-strongest sea surface temperature (SST) gradient between the equatorial central and western Pacific caused by the triple-dip La Niña and western Pacific warming. The convergent statistical and numerical evidence suggested that the enhanced SST gradients tend to amplify the western Pacific convection and the descending Rossby responses to the La Niña cooling, promoting the “seesaw” extreme pattern through the westward expansion of the western Pacific subtropical high (WPSH). Further investigation demonstrated that the magnitude of the YRV surface temperature and IB rainfall exhibited a reversed change from July to August. The persistent cooling of the southern Indian Ocean induced by the triple-dip La Niña increases the cross-equatorial moisture transport, which played a significant role in the record-breaking IB rainfall during July. By contrast, the historic YRV surface temperature occurred in August with a decrease in IB rainfall. The Barents–Kara Sea warming extended the downstream impact of the North Atlantic Oscillation via local air–sea interaction that enhanced the WPSH and the YRV extreme surface temperature by emanating an equatorward teleconnection wave train. The overlay of the tropical thermal conditions and extra-tropical forcings largely aggravated the severity of the “YRV drought and IB flood”.

Summer is the rainy season in East and South Asia. However, in 2022, the climatic pattern deviated from normal, showing contrasting extreme events in East and South Asia. The Yangtze River valley (YRV), which extends from the eastern Tibetan Plateau to coastal Shanghai, has suffered its most violent and persistent heat wave since 1979. Meanwhile, in Pakistan–northwestern India region, an unprecedented amount of rainfall occurred, causing severe flooding along the Indus Basin (IB). This “YRV drought and IB flood” pattern reflects the first MV-EOF mode of the surface air temperature (SAT) and precipitation over subtropical Asia (Supplementary Fig. 1), which accounts for about 17% of the total variance. The average temperature (precipitation) exceeds the climatology (1991–2020) mean by 2 K (150 mm) (Fig. 1a), which could equal as close as 2.5 standard deviations (σ) in 2022 (Fig. 1b). The co-occurrence of “seesaw” type extremes has posed major food security and health risks^{1,2}.

Concurrent with the “seesaw” extremes, the 5880-gpm contour dominates the mid-troposphere over the entire YRV, implying a pronounced westward expansion of the western Pacific subtropical high (WPSH) compared to its climatology mean (Fig. 1a). The resulting descending motion enhances incoming surface solar radiation by reducing cloud cover and facilitating the occurrence of heat waves^{3,4}. A large amount of anomalous lower-level southeasterly wind on the south flank of the WPSH extends to Pakistan–northern India⁵, conveying moisture air from the Bay of Bengal to fuel the increased IB rainfall (Fig. 1c).

The WPSH controls the summer climate over Asia, its variability can be modulated by the atmospheric and boundary layer forcings^{6–9}. For example, the condensational heating related to the South Asian summer monsoon rainfall may stimulate an anomalous upper-level South Asian high and downstream wave train propagating along the westerly jet to

¹Department of Atmospheric and Oceanic Sciences, and Institute of Atmospheric Sciences, and Shanghai Scientific Frontier Base of Ocean–Atmosphere Interaction, Fudan University, Shanghai 200438, China. ²Earth System Modeling Center, Nanjing University of Information Science and Technology, Nanjing, China. ³Department of Atmospheric Sciences, University of Hawaii at Manoa, Honolulu, HI, USA. ⁴Shanghai Typhoon Institute, China Meteorological Administration, Shanghai 200030, China. ✉e-mail: zhiweiwu@fudan.edu.cn

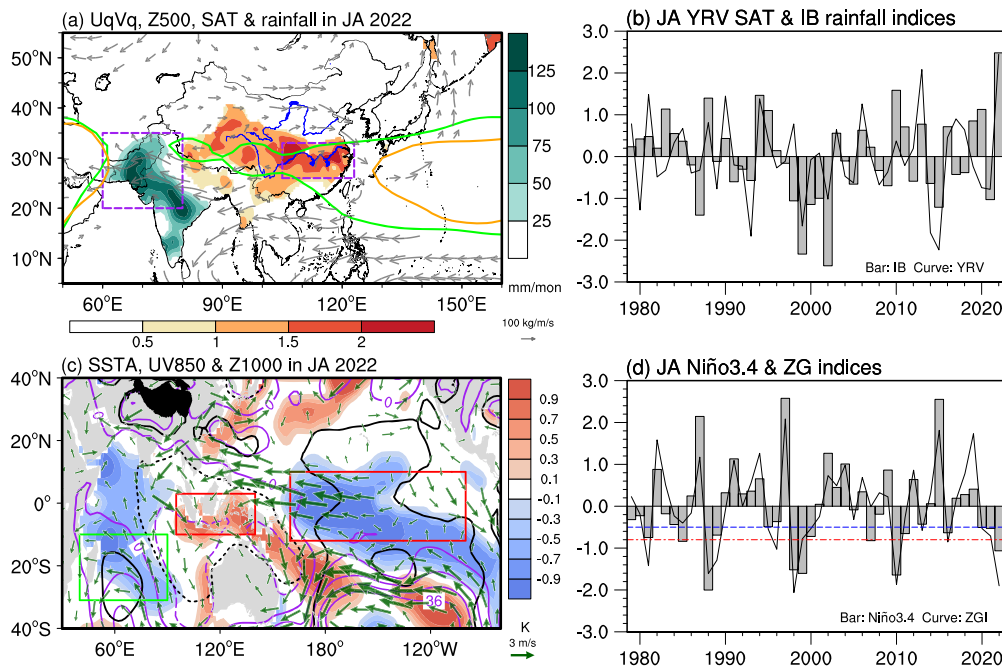


Fig. 1 | July–August 2022 climatic anomalies relative to the 1991–2020 climatology. **a** The column-integrated moisture flux ($UqVq$, vector, $\text{kg}\cdot\text{m}^{-1}\cdot\text{s}^{-1}$), Z500 (The green and orange contours represent 5880-gpm isoline for 2022 and climatology), surface air temperature (SAT; red shading, K), and precipitation (green shading, $\text{mm}\cdot\text{month}^{-1}$) anomalies in July–August 2022. The purple boxes imply the Yangtze River Valley (YRV, 27°N – 33°N , 105°E – 123°E) and Indus Basin (IB, 20°N – 35°N , 60°E – 80°E) domains. **c** SSTa (shading, K), UV850 (vector, $\text{m}\cdot\text{s}^{-1}$), and Z1000

(contour, m). The shading, vector, and black contour represent the region with anomalies' magnitude $>1\sigma$. The red boxes outline the tropical central-eastern (12°S – 10°N , 160°E – 260°E) and western (10°S – 3°N , 95°E – 140°E) Pacific. The green box frames the southern Indian Ocean (30°S – 10°S , 40°E – 90°E). Normalized time series of July–August **b** SAT averaged over YRV and precipitation averaged over IB, **d** Niño3.4 and zonal gradient indices from 1979 to 2022. Blue and red lines denote -0.5 and -0.8σ .

western North Pacific and North America^{10,11}, facilitating the zonal shift of WPSH with the meridional swing of East Asia westerly jet^{12–14}. Jin et al.¹⁵ found that the reduction in Barents sea ice promotes the development of cyclonic anomalies in the western North Pacific by a notable southeastward wave pattern¹⁵. The El Niño–Southern Oscillation (ENSO) has been recognized as a predominant contributor to the year-to-year variability of WPSH^{16,17}. The western Pacific cooling–Indian Ocean warming dipolar sea surface temperature (SST) anomalies maintain the WPSH through atmosphere–ocean interaction, prolonging the effect of El Niño to its decaying summer. The La Niña-associated tropical central Pacific cooling can enhance local subsidence, which in turn strengthens maritime continental convection through the east–west overturning circulation, enhancing WPSH by a direct Rossby response^{18,19}.

2022 is the third year of an infrequent and long-lasting triple-dip La Niña (Fig. 1d). Although the PC1 (-0.27 , $P < 0.1$), YRV temperature (-0.29 , $P < 0.1$), and IB precipitation (-0.33 , $P < 0.05$) indices show significant correlations with the July–August mean Niño-3.4 index, a moderate conventional La Niña ($\sim -1.1\sigma$) during the 2022 summer may struggle to fully explain such an extreme seesaw event. It also shows that the prominent negative SST anomalies located in the equatorial central Pacific (Fig. 1c) with the second-lowest Niño-4 index in July–August since 1979 (Supplementary Fig. 2a). Nevertheless, the composite of the YRV surface temperature and IB precipitation anomalies in the significant negative Niño-4 years did not exhibit an evident “seesaw” pattern resembling that of July–August 2022 (Supplementary Fig. 2b, c). This implies that equatorial central Pacific cooling may not directly contribute to the occurrence of the “YRV drought and IB flood”. Apart from the central and eastern Pacific cooling, it is worth noting that salient warming emerged in the western Pacific, largely enhancing the zonal SST gradient between the tropical western and central Pacific (Fig. 1c). The ENSO teleconnections vary with the intensity of the zonal SST gradient owing to the shift of the vertical motion location³⁰, even when the tropical central and eastern Pacific SSTAs are of similar magnitude^{21,22}. The ENSO with strong east–west SST contrast to a large

extent contributes to the occurrence of the regional^{23,24} and global monsoon^{25,26}, the Eurasian heatwave²⁷.

This study intends to compare the relative importance of La Niña with or without western Pacific warming in modulating the “seesaw” wet and dry conditions over South and East Asia. The ENSO signal can explain about one-third of heat wave variability over YRV in July–August, with the rest attributed to non-ENSO forcing and internal variability²⁸. From a broader perspective, we examine the superposition effect of the tropical and extra-tropical thermal forcings onto the “seesaw” event in the 2022 summer. The general conditions that favored the “seesaw” extreme pattern are introduced in “Results”. Then, we discussed the impact of southern Indian Ocean cooling to enhance IB rainfall in “Discussion”. “Methods” describes how the Extra-tropical factors aggregate the “seesaw” extremes. The summary and discussion are presented in the last part.

Results

The general conditions that favored the seesaw extreme pattern

The 2022 summer La Niña featured a prominent zonal SST gradient between western and central Pacific, ranking second in the past 40 years (Fig. 1c, d). The ENSO–East Asian winter monsoon relation changes with ENSO intensity and zonal SST gradient have been reported²³. Here, we compare the statistical connection of diverse La Niñas with the climatic anomalies over East and South Asia during the summertime. The La Niña events are defined as the SST anomalies in the Niño-3.4 region departure from its mean by less than -0.5 standard deviation (σ). Six strong gradient La Niñas (SGLN; 1981, 1988, 1989, 1998, 2010, and 2016) and seven weak gradient La Niñas (WGLN; 1985, 1999, 2000, 2007, 2011, 2020, and 2021) are selected according to the criteria that normalized zonal gradient index (ZGI) is less (larger) than -0.8σ . Changing the threshold of ZGI to -0.7σ or -0.9σ does not influence the qualitative results. The ZGI is defined as the SST difference between the tropical central Pacific (12°S – 10°N , 160°E – 260°E) and tropical western Pacific (10°S – 3°N , 95°E – 140°E). Although a relatively small region was selected in the tropical western Pacific, it encompasses part

of the warmest seas (the Indo-Pacific warm pool) of the world and is recognized as the “boiler box” of the Tropics²⁹. The Niño3.4 index exhibits an interannual time scale of variability, the peak is centered around 3–4 years. However, the spectral peaks of the ZGI are dominated by both interannual (3–4 years) and decadal (10 years) timescales (Supplementary Fig. 3). The results suggest that the two indices not only represent a diverse spatial pattern, but their time variations are also different.

We observed that the SGLN is featured by a salient east-west dipole distribution (Fig. 2a), which is reminiscent of the spatial pattern of mega-ENSO²⁵. The anomalous surface westerlies across Sumatra, remotely excited by central Pacific cooling, contribute to a reduction in local wind speed, warming the ocean in the west of the maritime continent and thereby enhancing the zonal SSTA gradient in the Pacific³⁰. The western Pacific warming and anomalous surface wind, however, vanishes during WGLN (Fig. 2d). Although the intensity of central Pacific cooling is comparable in two La Niña flavors, their associated tropical precipitation exhibits largely discrepancies in magnitude and scope. Compared with WGLN, the richer (poorer) precipitation covers a broader range of the central Pacific (Maritime Continent), suggesting a stronger Walker cell in SGLN.

Previous studies argued that the negative Indian Ocean SSTA is favored, but not controlled, by La Niña^{31–33}. However, there are no evident SST signals over the Indian Ocean based on the composition of the two La Niña flavors. Comparing the SSTAs associated with first-year (single) La Niñas and multiyear La Niñas, Jeong et al. suggested that multiyear La Niña is likely to further increase the chance of the Indian Ocean cooling development³⁴. Therefore, the presence of the first-year (single) La Niña in the two La Niña flavors, offsetting the potential impact of multiyear events, is likely a significant factor contributing to the neutral Indian Ocean SSTA.

It is interesting to note that above-normal SAT (rainfall) in the Yangtze River Valley (Indus Basin) emerges during SGLN (Fig. 2b, c), resembling the drought-flooding “seesaw” pattern in the 2022 summer (Fig. 1a). This is probably owing to the SGLN-associated WPSH elongating far westward to inland areas, acting as a “heat dome” to warm up the YRV region³, and the southeasterlies to the west flank of WPSH transporting moisture air to feed IB precipitation (Fig. 2a). However, the “seesaw” pattern (Fig. 2e, f) and the westward extent of WPSH (Fig. 2d) are not evident during WGLN.

The ECHAM5 model was applied to mimic the thermodynamic effect of WGLN and SGLN. In response to the SGLN forcing, the anomalous 500-hPa geopotential height (Z500) reinforced and extended further

westward, leading to a warmer YRV than that of the WGLN forcing (Fig. 3a, b). Meanwhile, the model reproduced both the excessive South Asian precipitation and the southeasterly moisture flow on the south side of WPSH, although the precipitation anomalies in the Indus Basin region are weaker than the observation (Fig. 3d, e). This implies that the “YRV drought and IB flood” events of 2022 are largely forced by the second-highest strong gradient La Niña.

Long-lasting La Niña induces southern Indian Ocean cooling to enhance IB rainfall

Despite the SGLN strength remained the same in July and August 2022, the seasonal expansion of the warm pool enhanced the atmosphere’s sensitivity to SST anomalies¹⁹, causing significant intensification of WPSH in August compared to July (Supplementary Fig. 4). As described in 3.1, Indus Basin rainfall can be fed by the southeasterly moisture flow on the south side of WPSH. However, the magnitude of Indus Basin rainfall reached the highest since 1979 in July and decreased in August (Fig. 4a, b). Why was the Indus Basin rainfall peaked in July and weakened with an enhancement of the WPSH?

Checking the SSTA distribution in Fig. 1c, we noticed that a negative Indian Ocean Dipole (IOD) concurred with SGLN in July–August 2022. Jeong et al. performed the pacemaker simulations and revealed that the westerly anomalies initially emerged in 2021 spring driving positive Bjerknes feedback to strengthen the negative IOD to develop a relatively extreme level in the 2022 summer³⁴. The SST cooling emerged in most regions of the Indian Ocean. The positive SST-precipitation relation over the southern Indian Ocean indicates SST driving the atmosphere^{35,36}, while the opposite situation occurred over the northern Indian Ocean (Supplementary Fig. 4). In July (Supplementary Fig. 4a and 4c), a contemporaneous prominent anomalous enhanced Mascarene high was observed just above the SST cooling in the southern Indian Ocean, concurred with below-normal rainfall and increased lower-level cross-equator Somali jets. The above-normal Mascarene high increased the hemispheric meridional surface pressure difference, and the resultant intense cross-equator Somali jet converged with the La Niña-associated southeasterly flow, causing uplifting to amplify the Indus Basin rainfall. However, the below-normal southern Indian Ocean rainfall was not evident in August, accompanied by the decrease of Mascarene high and the cross-equator jets (Supplementary Fig. 4b, d). This SST-rainfall relationship suggests that the anomalous

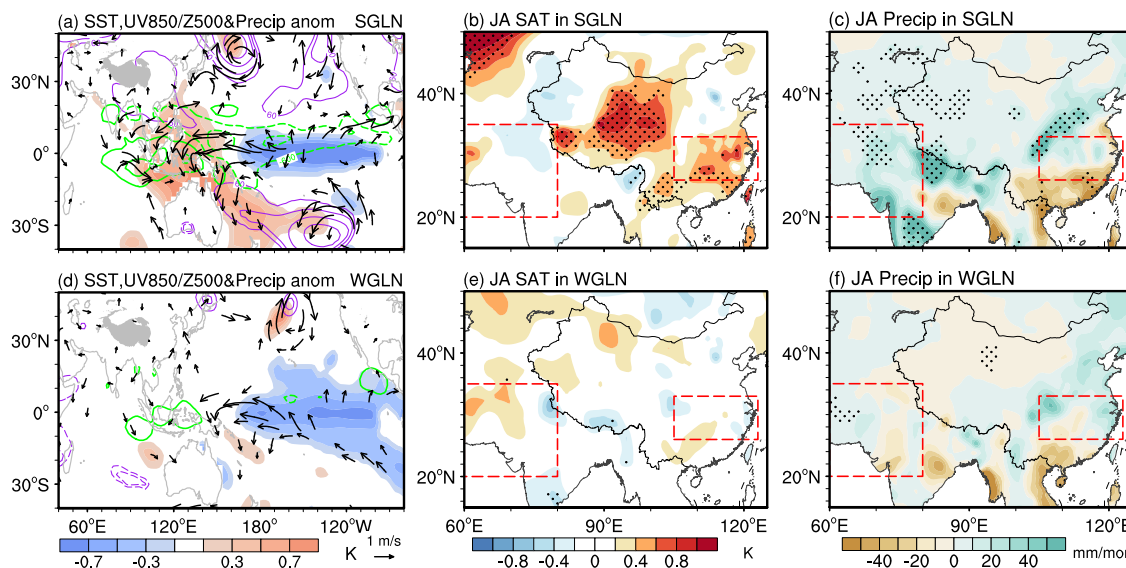


Fig. 2 | The different impacts of the two La Niña flavors. a SST (shading, K), UV850 (vector, $m\cdot s^{-1}$), Z500 (purple contour, m), and precipitation (green contour, $mm\cdot month^{-1}$), b surface air temperature (K), and c precipitation ($mm\cdot month^{-1}$) anomalies in July–August for strong gradient La Niña (SGLN). d, e, f the same as a, b, c except for weak gradient La Niña (WGLN). The anomalies that exceed the 95% confidence level (Student’s *t*-test) are displayed in a, d, represented by black dots in b, c, e, and f. The red boxes imply the Yangtze River Valley and Indus Basin domains.

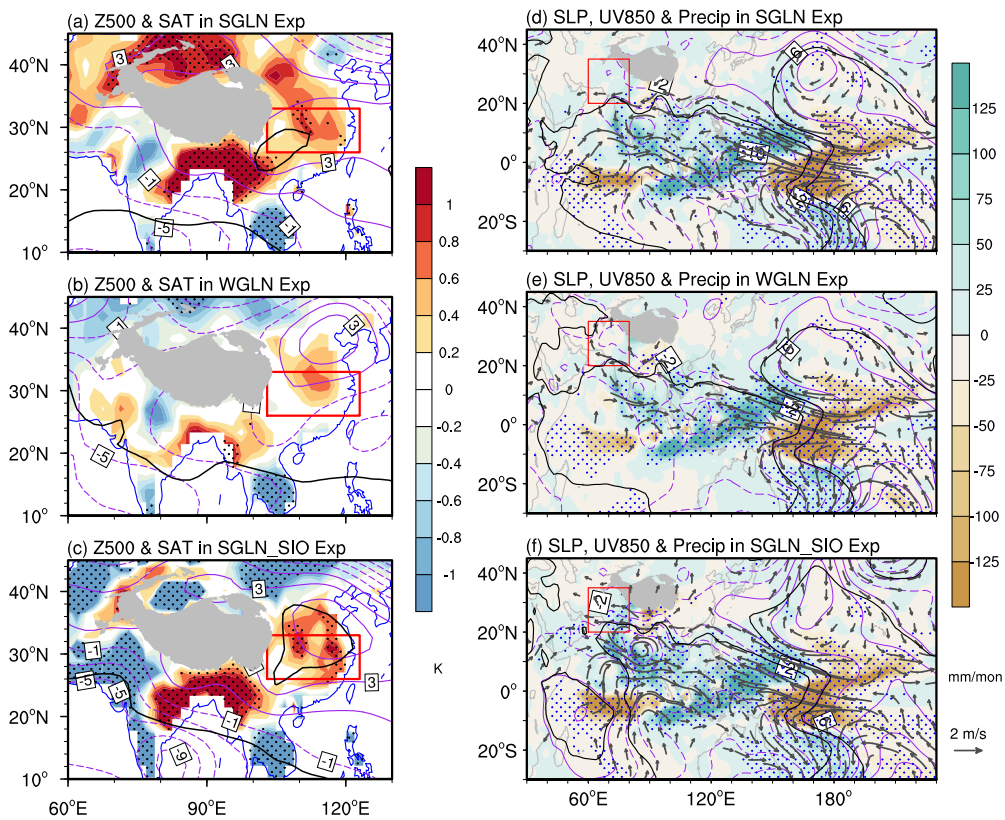


Fig. 3 | Atmospheric responses in ECHAM5 model. **a** SAT (shading, K) and Z500 (contour, m), **d** SLP (contour, hPa), UV850 (vector, $m\cdot s^{-1}$), and precipitation (shadings, $mm\cdot month^{-1}$) anomalies in SGLN run. The vector, dots, and thick black contour represent the region with anomalies exceeding the 90% confidence level (Student's *t*-test). **b**, **e** and **c**, **f** are the same as **a**, **d** but for WGLN and SGLN_SIO runs, respectively.

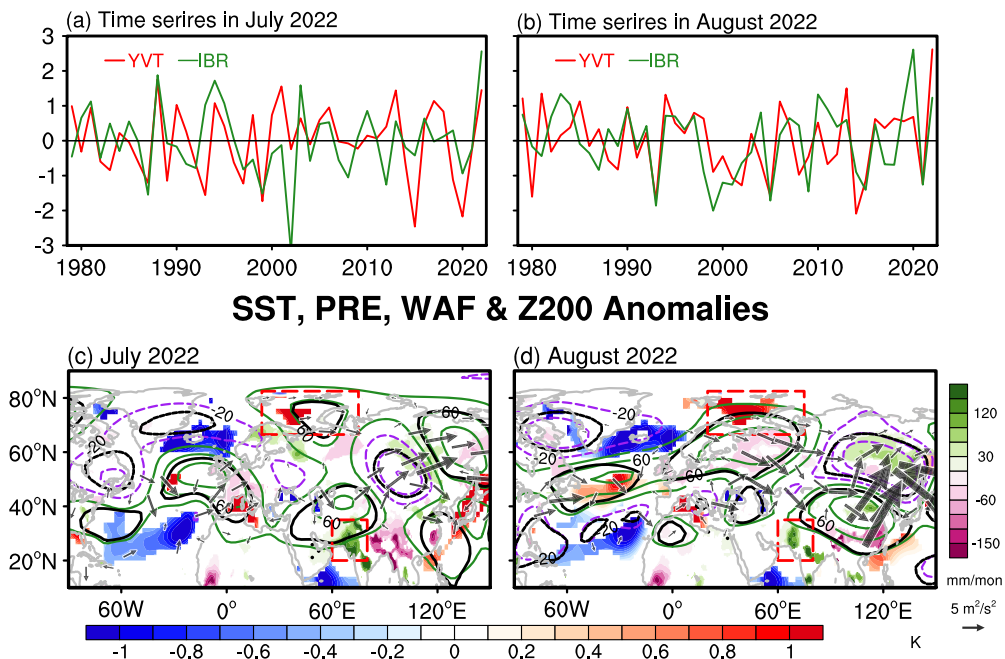


Fig. 4 | The July and August upper-tropospheric Rossby wave trains and associated energy propagation. **a** July and **b** August YRV SAT and IB rainfall indices from 1979 to 2022. 200-hPa wave activity flux (WAF200, vector, $m^2\cdot s^{-2}$), Z200 (contour, m), precipitation (green and purple shadings, $mm\cdot month^{-1}$), and SST (blue and red shadings, K) anomalies in **(c)** July 2022, **(d)** August 2022. The shading, vector, and thick black contour represent the region with anomalies exceeding 1σ . The red boxes imply the Brants-Kara Sea ($66^{\circ}N-82^{\circ}N$, $20^{\circ}E-70^{\circ}E$) and Indus Basin domains.

Mascarene high over the southern Indian Ocean is largely a consequence of underlying SST forcing due to diabatic cooling. We prescribed the southern Indian Ocean (SIO) cooling on the basis of SGLN simulation as the SGLN_SIO experiment. The ECHAM5 model largely simulated the observational results, including the westward extent of WPSH, the south-easterly flow from WP to South Asia, the enhanced Mascarene high, as well as the “YRV drought and IB flood” pattern (Fig. 3c, f). Moreover, the atmospheric responses are much stronger than those of the SGLN experiment, validating the importance of the southern Indian Ocean cooling in amplifying Indus Basin rainfall under the SGLN thermal conditions.

The western component of the SGLN has involved the tropical southeastern Indian Ocean, where the definition region of the eastern pole of the IOD³⁷. However, the negative SST-precipitation relation over the northern Indian Ocean has shifted the attention to the southern Indian Ocean, including the phenomena of the southern Indian Ocean cooling and Southern Indian Ocean Dipole (SIOD). The differences between SGLN_SIO and SGLN, and between SGLN_SIO and WGLN enable the contributions from the southern Indian Ocean cooling and the SIOD to be checked (Supplementary Fig. 5). Generally, the YRV surface temperature in response to southern Indian Ocean cooling and SIOD (Supplementary Fig. 5a and b) became significantly weaker after removing equatorial central Pacific cooling, while the positive rainfall anomalies (Supplementary Fig. 5c, d) remained pronounced over Indus Basin. The results indicate that the “seesaw” pattern can be reproduced when the southern Indian Ocean cooling or SIOD-like SSTAs are prescribed, with responses being more evident in the IB region.

The extra-tropical factors aggregate the “seesaw” extremes

Contrary to Indus Basin rainfall, the intensity of Yangtze River Valley temperature enhanced with WPSH (Fig. 4a, b), implying other specific factors besides the southern Indian Ocean cooling that contributed to the extreme YRV surface temperature. We noticed that an evident positive North Atlantic Oscillation (NAO) persisted from July to August 2022 through positive air-sea feedback with the underlying tripolar SSTA^{38,39}, but the downstream atmospheric circulation anomalies over Eurasia exhibited large discrepancies (Fig. 4c, d).

In July 2022, a circum-global teleconnection (CGT)-like pattern originated from Pakistan, propagating along the path of wave activity flux⁴⁰ (WAF) through central Asia to western Pacific (Fig. 4c). Such a “positive-negative-positive” CGT-like wave train represents a route for linking South and East Asian summer monsoons^{41–43}, of which the South Asian monsoon rainfall is considered a crucial driving factor^{10,44}. The linear baroclinic model experiment reproduces the observed upper-level circulation characteristics in July 2022. The 15-day averaged Z200 anomalies show a wave train pattern propagating along the Asian jet and accumulating in the jet exit region, forming a ridge near northeastern Asia⁴⁵ (Fig. 5a). Moreover, the observational and numerical evidence by Huang et al. proposed that the positive

NAO also extends its impact by exciting a downstream Rossby wave train propagating along the subtropical jet stream⁴⁶. This phenomenon leads to the fortification of the South Asian high, potentially contributing to the formation of the CGT-like pattern. We also found an anomalous high was situated further poleward, warming up the Barents-Kara Sea by enhancing surface radiative heating (Supplementary Fig. 6a). The northeastward propagated WAF anomalies originating from the anomalous Azores high and subsequently re-emerging over the Barents-Kara Sea, suggested a potential connection between this anomalous high and the positive NAO.

However, this anomalous high stretched southward with the north-eastward elongation of the NAO southern pole during August (Fig. 4d). A cross-Eurasian wave train propagated southeastward along the anomalous gradually intensifying WAF from the anomalous high over the Barents-Kara Sea and northern Europe region, crossing Balkhash Lake and extending all the way down to enhance WPSH. The two positive poles in this wave train contribute to the heatwave over the Arctic-Siberian plain (52°N–70°N, 30°E–60°E) and Yangtze River Valley in August 2022⁴⁷.

Kim et al. suggested the upper-level vorticity advection exciting the stationary anomalous high over the Arctic-Siberian plain. They emphasized that the anomalous high, coupled with underlying high SAT, further persists and amplifies itself by local positive land-air feedback⁴⁸. By contrast, we suggest that the positive feedback depends not only on the Arctic-Siberian plain SAT but also on the Barents-Kara Sea warming because the Barents-Kara warming became more evident during August, and may, in turn, drives the atmosphere by exciting upward heat flux (Supplementary Fig. 6b). The thermal forcing of Barents-Kara warming arguably slacked the poleward atmospheric thickness gradient with the increase of 1000–500-hPa thickness over the Barents-Kara Sea and northern Europe (Fig. 6a), thereby decreasing the mid-latitude Eurasian jet stream (Fig. 6b). A weaker jet stream tends to slow the eastward progression of the Rossby wave which favors the strengthening of the wave amplitude according to the Rossby wave theory⁴⁹. The decreased subpolar jet stream, therefore, follows a strengthened anomalous high (low) over the Barents-Kara Sea and northern Europe (Balkhash Lake-Mongolia) region. The westerly anomalies on the south flank of the anomalous low over the Balkhash Lake-Mongolia region strengthen the East Asian jet (Fig. 6b) and the WPSH (Fig. 4d).

The assertion is identified by the ECHAM5 model derived by the Barents-Kara warming, which to some extent simulated the northeastward elongation of the NAO southern pole and the southeastward propagation of the cross-Eurasian wave train along the upper-level WAF anomalies from the Barents-Kara Sea and northern Europe across Balkhash Lake to the YRV (Fig. 5b), although the center of anomalous Barents-Kara Sea and northern Europe high shift westward slightly compared to the observed counterparts (Fig. 4d). The Barents-Kara Sea warming decreased the meridional 1000–500-hPa thickness gradient (Fig. 6c) to mitigate (accelerate) the two branches of the mid-latitude Eurasian jets (Fig. 6d), finally enhancing WPSH to rise up YRV temperature. The processes also proved that summer

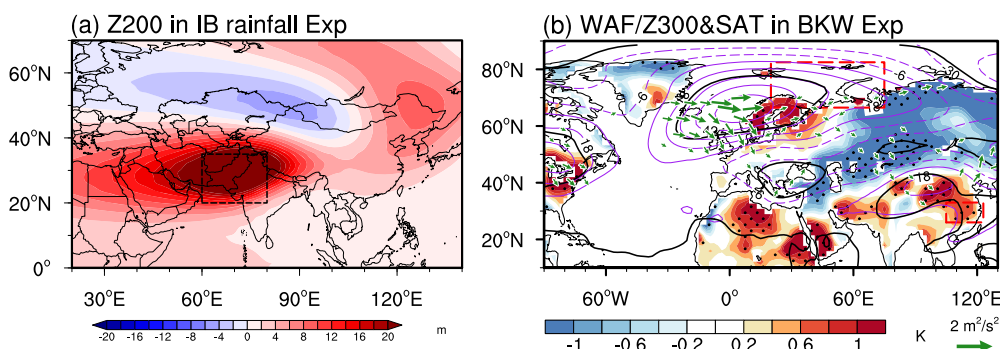


Fig. 5 | Atmospheric response in LBM and ECHAM5 models. a Z200 (contour, m) anomalies in response to Indus Basin precipitation forcing in LBM. **b** 300-hPa WAF (vector, $m^2 s^{-2}$), geopotential height (Z300, contour, m), and SAT (shadings, K)

anomalies in responses to Barents-Kara warming (BKW) forcing in ECHAM5. The vector, black contour, and dots represent the region with anomalies significant at the 90% confidence level (Student’s *t* test).

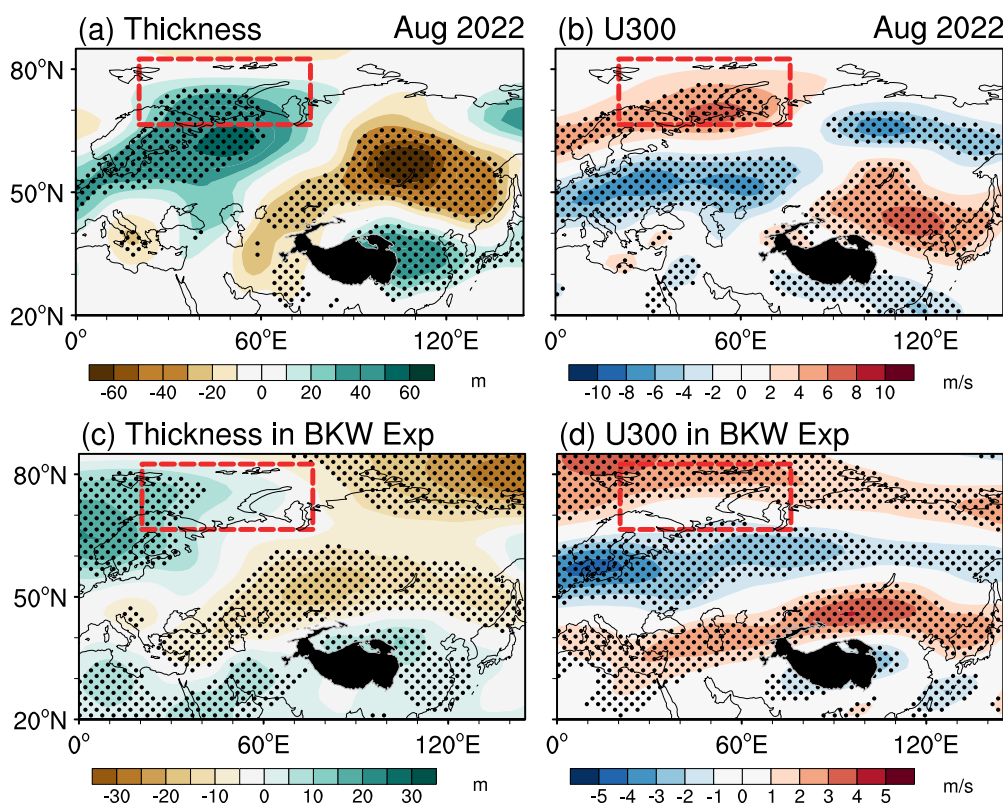


Fig. 6 | The Barents-Kara Sea warming forced atmospheric anomalies. **a** 1000–500-hPa thickness (m), **b** U300 (m s^{-1}) anomalies in August 2022. **b**, **d** the same as **a**, **c** except for response to Barents-Kara warming forcing in EHCAM5. The

dots in (**a**, **b**) represent the region with anomalies' magnitude $> 1\sigma$, in (**c**, **d**) represent the region with anomalies significant at the 90% confidence level (Student's t test). Black shading denotes the Tibetan Plateau.

1000–500-hPa thickness variability over Eurasia thermodynamically expressed the upper-tropospheric westerly variability and significantly correlated with Arctic warming and sea ice loss⁵⁰. Therefore, except for the SGLN, the forcing of Barents-Kara warming connecting NAO with the cross-Eurasian wave train also largely contributed to the increase of YRV SAT in August 2022. However, the WAF anomalies (Fig. 5c), in contrast to their observational counterparts (Fig. 4d), weaken gradually during their southeastward propagation. This is probably due to the fact that AGCM cannot capture the local land-surface feedback that enhances the geopotential and horizontal wind perturbation. A coupled model is called for applying in the follow-up research.

Discussion

We presented consistent observational and simulated evidence to demonstrate that a significant SST gradient between the tropical central and western Pacific, referred to as a strong-gradient La Niña, provides favorable conditions for the “Yangtze River Valley (YRV) drought and Indus Basin (IB) flood” seesaw extreme pattern during 1979–2022 and in July–August 2022 in particular. We reveal that the long-lasting 2020–2022 La Niña-induced southern Indian Ocean cooling further enhanced the cross-equatorial moisture transport, leading to record-breaking Indus Basin rainfall in July 2022. The Indus Basin rainfall further excited a circum-global teleconnection-like pattern to heat YRV (Fig. 7a). In addition, in August 2022, the Barents-Kara Sea warming extended the NAO southern pole towards northern Europe via local air-sea feedback. The downstream impact of NAO excites a southward propagation of the Rossby wave train, adding to the historic heat wave over the YRV (Fig. 7b).

The intensification and extreme westward expansion of the WPSH was the fundamental factor linking the “seesaw” extreme pattern to both tropical and extra-tropical forcings. Beyond the conventional understanding that the central Pacific variability affects WPSH, we demonstrated that the western Pacific warming in strong-gradient La Niña profoundly enhanced the

maritime continental convection, thereby strengthening the WPSH through amplifying the central Pacific cooling-excited descending Rossby wave. This suggests that the east-west contrast in La Niña SSTAs could be a valuable source of predictability for seasonal prediction of the “YRV drought and IB flood”. The heat wave variability over YRV in July–August is also partially explained by non-ENSO forcing and internal variability²⁸. However, the extra-tropical teleconnections varied between July and August 2022 in contrast to the steady tropical thermal forcings. Investigating the reasons behind this month-to-month variation in extra-tropical teleconnections can enhance our understanding of developing and sustaining mechanisms for extreme climatic events.

We also constructed the multi-regression model to estimate the contributions of the SST gradient over the tropical Pacific Ocean and extra-tropical forcings (See details in “Methods”). Despite that the statistical models capture a positive anomaly of the seesaw pattern in 2022, it estimates the observed anomaly by about half (0.85 vs. 1.95; 44%) in July (Fig. 7c), by about one-third (0.55 vs. 1.9; 28%) in August (Fig. 7d). The underestimated magnitude of the “YRV drought and IB flood” seesaw index suggests that other physical processes independent of the tropical Pacific zonal SST gradient, the southern Indian Ocean and Barents-Kara Sea forcings were at work as well. For instance, Liu et al. emphasized that the 2022 YRV heatwave was also embedded in intra-seasonal oscillation (ISO)⁵¹. The relationship of ISO with extreme Indus Basin rainfall deserves further investigation. Moreover, as revealed by the previous study, the surface climatic conditions also contributed by local land-atmosphere interaction^{52,53}. Detecting the potential local positive feedback that maintains the extreme IB rainfall or YRV surface temperature is also of significant interest.

Methods

Reanalysis datasets

The Monthly Extended Reconstructed Sea Surface Temperature version 5 (ERSSTv5) data⁵⁴ for 1979–2022 was obtained from the National Oceanic

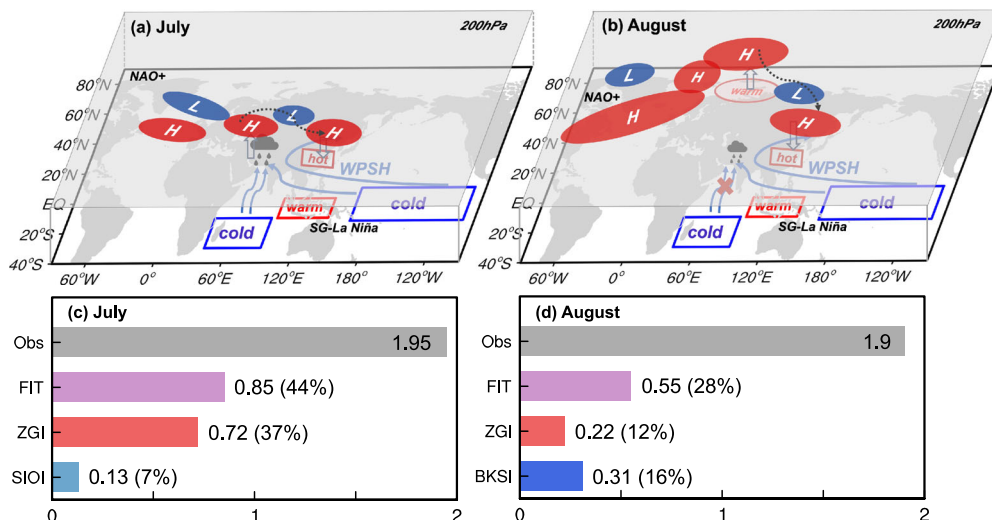


Fig. 7 | A schematic diagram demonstrating the mechanism of “seesaw” extremes in July and August 2022. The blue and red centers at the upper-level represent the CGT-like pattern in (a), and the cross-Eurasian wave train in (b) respectively, and the dotted arrow represents the propagation of WAF. The warm and cold centers in the Pacific refer to the zonal SST gradient. The cold center in the SIO excited strong

cross-equator flow which is denoted by the blue double arrow. See the text for details. **c, d** These present the observed anomalous “YRV drought and IB flood” seesaw in 2022 and the parts explained by different components of the statistical model in July and August, respectively.

and Atmospheric Administration (NOAA), with a horizontal resolution of $2^\circ \times 2^\circ$; The monthly precipitation data for 1979–2022 from NOAA’s Land Precipitation Reconstruction (PREC/L) data set⁵⁵; The monthly surface air temperature data on a $0.5^\circ \times 0.5^\circ$ grid from the Global Historical Climatology Network version 2 and the Climate Anomaly Monitoring System (GHCN_CAMS)⁵⁶ for 1979–2022; and the monthly atmospheric reanalysis data on a $1.5^\circ \times 1.5^\circ$ grid from the fifth-generation of ECMWF global atmospheric reanalysis (EAR5) data set⁵⁷ for 1979–2022.

Methodology

In this study, the main statistical methods include correlated coefficient analysis, linear regression analysis, and composite analysis. The statistical significance test is based on a two-tailed Student’s *t* test with $N-2$ degree of freedom (N is the number of years). Monthly anomalies refer to the deviations from the climatological mean (1991–2020) with the linear trend removed.

We established the covariance matrix of the surface air temperature (SAT) and precipitation anomalies in subtropical Asia ($20^\circ\text{N}-40^\circ\text{N}$, $105^\circ\text{E}-123^\circ\text{E}$) from 1979 to 2022 to perform the multivariate empirical orthogonal function (MV-EOF) analysis.

The Niño-3.4 and Niño-4 indices were obtained from the Climate Prediction Center. The zonal gradient index is defined as the SST difference between the tropical central Pacific ($12^\circ\text{S}-10^\circ\text{N}$, $160^\circ\text{E}-260^\circ\text{E}$) and tropical western Pacific ($10^\circ\text{S}-3^\circ\text{N}$, $95^\circ\text{E}-140^\circ\text{E}$). And the normalized precipitation and SAT averaged over ($20^\circ\text{N}-35^\circ\text{N}$, $60^\circ\text{E}-80^\circ\text{E}$) and ($27^\circ\text{N}-33^\circ\text{N}$, $105^\circ\text{E}-123^\circ\text{E}$) were defined as the Indus Basin rainfall and YRV SAT indices.

To assess the impacts of the tropical and extra-tropical SST forcing, the 5th generation European Center-Hamburg model (ECHAM5.4)⁵⁸, was used for the numerical experiment. The ECHAM5.4 model was developed by the Max-Planck Institute and has been widely used in previous studies to understand the impact processes and mechanisms of ENSO and Arctic sea ice/SST^{15,21–23,59}. All the simulations utilized the triangular 63 horizontal resolution ($1.9^\circ \times 2.5^\circ$) with 19 vertical levels. The control (CTRL) experiment was driven by the observed climatology SST. We carried out 40-year integration and the last 30 years were extracted for analysis. The sensitivity experiments were integrated for 30 years with initial conditions obtained from the CTRL run and the specific SSTA in July–August 2022 prescribed onto the July and August climatological SST.

The linear baroclinic model (LBM) was also performed to investigate the linear response of the circulation anomaly over Eurasia to the Indus Basin diabatic heating anomaly with 128×64 horizontal grids and 20 sigma vertical levels. This model was developed by the Center for Climate System Research at the University of Tokyo and the National Institute for Environmental Studies in Japan⁶⁰. The forcing of the diabatic heating is parameterized by the observational July precipitation anomalies over the Indus Basin region ($20^\circ-35^\circ\text{N}$, $60^\circ-80^\circ\text{E}$). We integrated the LBM for 30 days and averaged outputs for the last 15 days as the stationary atmospheric responses. The added forcings are displayed in Supplementary Fig. 7 in supplementary.

Considering the seesaw pattern was impacted by different extra-tropical forcings in the two months, we quantitatively diagnose the contribution of the SST gradient over the tropical Pacific Ocean and extra-tropical forcings in July and August, respectively. To represent the variability of the seesaw pattern, we defined a “YRV drought and IB flood” seesaw index as:

$$YISI = 0.5 \times (\text{YRV SAT index} + \text{IB rainfall index}) \quad (1)$$

We construct the multi-regression model based on the standardized zonal gradient (ZGI), southern Indian Ocean (SIOI), and Barents-Kara Sea (BKSI) indices:

$$YISI_{Jul} = -0.36 \times ZGI_{Jul} - 0.1 \times SIOI_{Jul} \quad (2)$$

$$YISI_{Aug} = -0.11 \times ZGI_{Aug} - 0.28 \times BKSI_{Aug} \quad (3)$$

Data availability

The ERA5 data are available from the European Centre for Medium-Range Weather Forecasts (ECMWF) website (<https://www.ecmwf.int/en/forecasts/dataset/ecmwf-reanalysis-v5>). The ERSST and PRECL data, the Niño3.4 and Niño-4 indices are obtained from the NOAA website (<https://psl.noaa.gov/data>). The GHCN_CAMS are downloaded from the GHCN website (<https://www.ncdc.noaa.gov/products/land-based-station/global-historical-climatology-network-daily>).

Code availability

All figures in this paper are produced by NCL version 6.6.2, and the source codes can be obtained upon request to the first author.

Received: 20 October 2023; Accepted: 15 February 2024;

Published online: 26 February 2024

References

- Du, H. & Zhou, F. Mitigating extreme summer heat waves with the optimal water-cooling island effect based on remote sensing data from Shanghai, China. *Int. J. Environ. Res.* **19**, 9149 (2022).
- Devi, S. Pakistan floods: Impact on food security and health systems. *Lancet* **400**, 799–800 (2022).
- Gao, M., Wang, B., Yang, J. & Dong, W. Are peak summer sultry heat wave days over the Yangtze–Huaihe River Basin predictable. *J. Clim.* **31**, 2185–2196 (2018).
- Choi, N., Lee, M., Cha, D., Lim, Y. & Kim, K. Decadal changes in the interannual variability of heat waves in east Asia caused by atmospheric teleconnection changes. *J. Clim.* **33**, 1505–1522 (2019).
- Hong, C.-C., Lu, M.-M. & Kanamitsu, M. Temporal and spatial characteristics of positive and negative Indian Ocean dipole with and without ENSO. *J. Geophys. Res.* **113**, D08107 (2008).
- Yang, R., Xie, Z. & Cao, J. A dynamic index for the westward ridge point variability of the western Pacific subtropical high during summer. *J. Clim.* **30**, 3325–3341 (2017).
- Wang, B., Bao, Q., Hoskins, B., Wu, G. & Liu, Y. Tibetan Plateau warming and precipitation changes in East Asia. *Geophys. Res. Lett.* **35**, L14702 (2008).
- Wu, Z., Li, J., Jiang, Z. & Ma, T. Modulation of the Tibetan Plateau snow cover on the ENSO teleconnections: from the East Asian Summer Monsoon perspective. *J. Clim.* **25**, 2481–2489 (2012).
- Zhou, Z.-Q., Xie, S.-P. & Zhang, R. Historic Yangtze flooding of 2020 tied to extreme Indian Ocean conditions. *Proc. Natl Acad. Sci. USA* **118**, e2022255118 (2021).
- Ding, Q. & Wang, B. Circumglobal teleconnection in the Northern Hemisphere Summer. *J. Clim.* **18**, 3483–3505 (2005).
- Zhang, Y. Z. et al. Climatic effects of the Indian Ocean Tripole on the Western United States in Boreal Summer. *J. Clim.* **35**, 2503–2523 (2022).
- Wei, W., Zhang, R., Wen, M., Rong, X. & Li, T. Impact of Indian summer monsoon on the south Asian high and its influence on summer rainfall over China. *Clim. Dyn.* **43**, 1257–1269 (2014).
- Chen, X. et al. Emergent constraints on future projections of the western North Pacific Subtropical High. *Nat. Commun.* **11**, 2802 (2020).
- Tang, S. et al. Linkages of unprecedented 2022 Yangtze River Valley heatwaves to Pakistan flood and triple-dip La Niña. *npj Clim. Atmos.* **6**, 44 (2023).
- Jin, R., Yu, H., Wu, Z. & Zhang, P. Impact of the North Atlantic sea surface temperature tripole on the Northwestern Pacific weak tropical cyclone frequency. *J. Clim.* **35**, 3057–3074 (2022).
- Sui, C. H., Chung, P. H. & Li, T. Interannual and interdecadal variability of the summertime western North Pacific subtropical high. *Geophys. Res. Lett.* **34**, L11701 (2007).
- Wu, B. & Zhou, T. Oceanic origin of the interannual and interdecadal variability of the summertime western Pacific subtropical high. *Geophys. Res. Lett.* **35**, L13701 (2008).
- Wang, B., Xiang, B. & Lee, J.-Y. Subtropical high predictability establishes a promising way for monsoon and tropical storm predictions. *PNAS* **110**, 2718–2722 (2013).
- Xiang, B., Wang, B., Yu, W. & Xu, S. How can anomalous western North Pacific subtropical high intensify in late summer? *Geophys. Res. Lett.* **40**, 2349–2354 (2013).
- Hoell, A. & Funk, C. The ENSO-related West Pacific Sea surface temperature gradient. *J. Clim.* **26**, 9545–9562 (2013).
- Zhang, P., Wang, B. & Wu, Z. Weak El Niño and winter climate in the mid-high latitude Eurasia. *J. Clim.* **32**, 402–421 (2019).
- Zhang, P. & Wu, Z. Reexamining the connection of El Niño and North American winter climate. *Int. J. Climatol.* **40**, 6133–6144 (2021).
- Zhang, P., Wu, Z. & Li, J. Reexamining the relationship of La Niña and the east Asian winter monsoon. *Clim. Dyn.* **53**, 779–791 (2019).
- Li, J. & Wang, B. Predictability of summer extreme precipitation days over eastern China. *Clim. Dyn.* **51**, 4543–4554 (2018).
- Wang, B. et al. Northern Hemisphere summer monsoon intensified by mega-El Niño/southern oscillation and Atlantic multidecadal oscillation. *Proc. Natl Acad. Sci. USA* **110**, 5347–5352 (2013).
- Wang, B. et al. Toward predicting changes in the land monsoon rainfall a decade in advance. *J. Clim.* **31**, 2699–2714 (2018).
- Zhou, Y. & Wu, Z. Possible impacts of mega-El Niño/Southern Oscillation and Atlantic multidecadal oscillation on Eurasian heat wave frequency variability. *Q. J. R. Meteorol. Soc.* **142**, 1647–1661 (2016).
- Chen, X. & Zhou, T. Relative contributions of external SST forcing and internal atmospheric variability to July–August heat waves over the Yangtze River valley. *Clim. Dyn.* **51**, 4403–4419 (2018).
- Ramage, C. S. Role of a tropical “Maritime Continent” in the atmospheric circulation. *Mon. Weather Rev.* **96**, 365–370 (1968).
- Hendon, H. H. Indonesian rainfall variability: impacts of ENSO and local air-sea interaction. *J. Clim.* **16**, 1775–1790 (2003).
- Abram, N. J. et al. Coupling of Indo-Pacific climate variability over the last millennium. *Nature* **579**, 385–392 (2020).
- Du, Y. et al. Thermocline warming induced extreme Indian Ocean dipole in 2019. *Geophys. Res. Lett.* **47**, e2020GL090079 (2020).
- Wang, G., Cai, W., Yang, K., Santoso, T. & Yamagata, T. A unique feature of the 2019 extreme positive Indian Ocean dipole event. *Geophys. Res. Lett.* **47**, e2020GL088615 (2020).
- Jeong, H., Park, H., Chowdary, J. S. & Xie, S. Triple-Dip La Niña contributes to Pakistan flooding and Southern China drought in summer 2022. *Bull. Am. Meteorol. Soc.* **104**, E1570–E1586 (2023).
- Kumar, A., Zhang, L. & Wang, W. Sea surface temperature–precipitation relationship in different reanalyses. *Mon. Weather Rev.* **141**, 1118–1123 (2013).
- Lu, R. & Lu, S. Local and remote factors affecting the SST–precipitation relationship over the western North Pacific during summer. *J. Clim.* **27**, 5132–5147 (2014).
- Saji, N. H., Goswami, B. N., Vinayachandran, P. N. & Yamagata, T. A dipole mode in the tropical Indian Ocean. *Nature* **401**, 360–363 (1999).
- Wu, Z., Wang, B., Li, J. & Jin, F. F. An empirical seasonal prediction model of the East Asian summer monsoon using ENSO and NAO. *J. Geophys. Res.* **114**, D18120 (2009).
- Li, J. P., Zheng, F., Sun, C., Feng, J. & Wang, J. Pathways of influence of the northern hemisphere mid–high latitudes on East Asian climate: a review. *Adv. Atmos. Sci.* **36**, 902–921 (2019).
- Takaya, K. & Nakamura, H. A formulation of a phase-independent wave-activity flux for stationary and migratory quasigeostrophic eddies on a zonally varying basic flow. *J. Atmos. Sci.* **58**, 608–627 (2001).
- Ding, Q.-H., Wang, B. & Wallace, M. Tropical-extratropical teleconnections in boreal summer: observed interannual variability. *J. Clim.* **24**, 1878–1896 (2011).
- Liu, G., Wu, R., Sun, S. & Wang, H. Synergistic contribution of precipitation anomalies over northwestern India and the South China Sea to high temperature over the Yangtze River Valley. *Adv. Atmos. Sci.* **32**, 1255–1265 (2015).
- Huang, R. et al. Differences and links between the East Asian and South Asian summer monsoon systems: characteristics and variability. *Adv. Atmos. Sci.* **34**, 1204–1218 (2017).
- Rodwell, M. & Hoskins, B. Monsoons and the dynamics of deserts. *Q. J. R. Meteorol. Soc.* **122**, 1385–1404 (1996).

45. Enomoto, T., Hoskins, B. J. & Matsuda, Y. The formation mechanism of the Bonin high in August. *Q. J. R. Meteorol. Soc.* **129**, 157–178 (2003).
 46. Huang, H., Zhu, Z. & Li, J. Disentangling the unprecedented Yangtze River Basin extreme high temperatures in summer 2022: combined impacts of the re-intensified La Niña and strong positive NAO. *J. Clim.* **37**, 927–942 (2024).
 47. Wang, Z., Luo, H. & Yang, S. Different mechanisms for the extremely hot central-eastern China in July–August 2022 from a Eurasian large-scale circulation perspective. *Environ. Res. Lett.* **18**, 024023 (2023).
 48. Kim, J. H., Kim, S. J., Kim, J. H., Hayashi, M. & Kim, M. K. East Asian heatwaves driven by Arctic–Siberian warming. *Sci. Rep.* **12**, 18025 (2022).
 49. Palmén, E., Newton, C. W. Atmospheric Circulation Systems, International Geophysics Series, 13. (Academic, 1969).
 50. Wu, B. & Francis, J. A. Summer Arctic cold anomaly dynamically linked to East Asian heatwaves. *J. Clim.* **32**, 1137–1150 (2019).
 51. Liu, B., Zhu, C., Ma, S., Yan, Y. & Jiang, N. Subseasonal processes of triple extreme heatwaves over the Yangtze River Valley in 2022. *Weather. Clim. Extremes* **40**, 100572 (2023).
 52. Koster, R. et al. Regions of strong coupling between soil moisture and precipitation. *Science* **305**, 338–340 (2004).
 53. Mueller, B. & Seneviratne, S. Hot days induced by precipitation deficits at the global scale. *Proc. Natl Acad. Sci. USA* **109**, 12398–12403 (2012).
 54. Huang et al. Extended reconstructed sea surface temperature, version 5 (ERSSTv5): upgrades, validations, and intercomparisons. *J. Clim.* **30**, 8179–8205 (2017).
 55. Chen, M., Xie, J. E., Janowiak, P. & Arkin, P. A. Global land precipitation: a 50-yr monthly analysis based on gauge observations. *J. Hydrometeorol.* **3**, 249–266 (2002).
 56. Fan, Y. & Van den Dool, H. A global monthly land surface air temperature analysis for 1948–present. *J. Geophys. Res. Atmos.* **113**, D01103 (2008).
 57. Hersbach, H. et al. The ERA5 global reanalysis. *Q. J. R. Meteorol. Soc.* **146**, 1999–2049 (2020).
 58. Roeckner, E. et al. The atmospheric general circulation model ECHAM5. Part I: model description. *Max Planck Inst. Rep.* **349**, 140 pp (2003).
 59. Zhang, P., Wu, Z. & Jin, R. How can the winter North Atlantic Oscillation influence the early summer precipitation in Northeast Asia: effect of the Arctic sea ice. *Clim. Dyn.* **56**, 1989–2005 (2021).
 60. Watanabe, M. & Kimoto, M. Atmosphere–ocean thermal coupling in the North Atlantic: a positive feedback. *Q. J. R. Meteorol. Soc.* **126**, 3343–3369 (2000).
- National Natural Science Foundation of China (NSFC) Major Research Plan on West-Pacific Earth System Multi-spheric Interactions (Grant No. 92158203), the Ministry of Science and Technology of China (Grant No. 2023YFF0805100), and the Second Tibetan Plateau Scientific Expedition and Research (STEP) program (Grant No. 2019QZKK0102), the National Science Foundation of Climate Dynamics Division Award (No. AGS-2025057). S.S.L. was supported by the Institute for Basic Science (IBS), Republic of Korea, under IBS-R028-D1. This is publication No. 418 of Earth System Modeling Center (ESMC).

Author contributions

Peng Zhang and Zhiwei Wu designed the study. The data collection, data analysis, and model designments were performed by Peng Zhang, Rui Jin, and Can Cao. The first draft of the manuscript was written by Peng Zhang. Bin Wang, Zhiwei Wu reviewed the manuscript.

Competing interests

The authors declare no competing interests.

Additional information

Supplementary information The online version contains supplementary material available at <https://doi.org/10.1038/s41612-024-00597-2>.

Correspondence and requests for materials should be addressed to Zhiwei Wu.

Reprints and permissions information is available at <http://www.nature.com/reprints>

Publisher's note Springer Nature remains neutral with regard to jurisdictional claims in published maps and institutional affiliations.

Open Access This article is licensed under a Creative Commons Attribution 4.0 International License, which permits use, sharing, adaptation, distribution and reproduction in any medium or format, as long as you give appropriate credit to the original author(s) and the source, provide a link to the Creative Commons licence, and indicate if changes were made. The images or other third party material in this article are included in the article's Creative Commons licence, unless indicated otherwise in a credit line to the material. If material is not included in the article's Creative Commons licence and your intended use is not permitted by statutory regulation or exceeds the permitted use, you will need to obtain permission directly from the copyright holder. To view a copy of this licence, visit <http://creativecommons.org/licenses/by/4.0/>.

© The Author(s) 2024

Acknowledgements

The authors wish to thank anonymous referees' comments that led to a much-improved manuscript. This research was jointly supported by the